

Bioinspired maskless structural colour patterning via tunable nanoparticle segregation

Received: 12 November 2025

Accepted: 27 February 2026

Published online: 17 March 2026

 Check for updates

Li Yang¹, Yujie Peng¹, Zhe Wang¹, Wei Wang², Yuechuan Wang^{1,3} & Ming Xiao^{1,3}✉

Structural colouration arises from the interaction of light with nanoscale structures and offers sustainable alternatives to pigment-based colours. However, current structural colour patterning methods rely on multi-step lithographic processes or multiple ink formulations, limiting scalability and spatial resolution. Inspired by melanosome self-assembly in bird feathers, we develop a one-step, mask-free strategy to generate high-resolution structural colour patterns via tunable nanoparticle segregation. During photocuring, silica nanoparticles dispersed in acrylic resin migrate toward oxygen-permeable substrates, forming a nanoparticle-enriched disordered layer. Such segregation is driven by interfacial oxygen inhibition and kinetically governed by the photocuring rate. Using grayscale digital light processing printing, we programmably control the local segregation thickness to create high-resolution structural colour patterns for visual display and information encryption. The segregation structure also affects mid-infrared reflectivity, allowing for infrared camouflage. This scalable approach establishes a mechanistically guided route to multifunctional photonic materials.

Structural colours are generated by reflection of specific wavelengths of light from periodic or aperiodic micro/nano-structures, offering environmentally friendly alternatives to pigment-based colouration^{1,2}. Structural colour patterning can be widely used in decoration³, anti-counterfeiting^{4–6}, information encryption^{7,8}, camouflage^{9,10}, sensor^{11,12}, and display^{13,14}. However, conventional structural colour patterning typically relies on lithography-like strategies, where unmasked regions with initial nanostructures are first photocured, followed by immobilization of masked regions with different nanostructures. To adjust nanostructures for different colours, external stimuli such as magnetic fields^{15,16}, electric fields¹⁷, temperature⁶, or solvents⁴ are applied upon curing to locally manipulate the arrangements of assembly units (nanoparticle, liquid crystal, block copolymer, etc.). These approaches require physical masks and multiple photocuring steps, limiting scalability and spatial resolution. A one-step, mask-free strategy for

precisely controlling local nanostructures remains a key challenging in advancing structural colour patterning.

Printing technology has been used to fabricate structurally coloured materials with high flexibility and customization^{18–20}. However, printing various colours often requires multiple resin formulations across methods such as inkjet printing, direct ink writing, or vat photopolymerization^{3,18,21–24}. To the best of our knowledge, only a few studies have preliminarily explored the concept of printing different colours using a single ink. Two-photon printing can locally customize the periodic nanostructures for structural colour patterns^{25,26}, but suffers from low throughput and high cost. Li et al. inkjet printed a full spectrum of structural colours by controlling the sizes of printed microdomes to tuning their total internal reflections (TIR)²⁷. These TIR-based colours can only be observed from the backside of the printed samples. Liao et al. achieved spatial colour contrast in printed colloidal

¹College of Polymer Science and Engineering, Sichuan University, Chengdu, China. ²College of Physics, Sichuan University, Chengdu, China. ³State Key Laboratory of Advanced Polymer Materials, Sichuan University, Chengdu, China. ✉e-mail: mingxiao@scu.edu.cn

photonic crystal hydrogels by locally tuning the amount of cured monomers and the cross-linking density²⁸. Jeon et al. used direct ink writing of bottlebrush block copolymer solutions and printed different colours via kinetically trapping distinct nanostructures during the evaporation-driven self-assembly²⁹. These methods are limited to hydrogel or bottlebrush polymeric systems and offer relatively low resolution, with printed pattern features typically on the millimetre scale. It remains challenging to fabricate high-resolution structural colour patterns from a single ink via printing technology.

Nanoparticle segregation or stratification offers a route to spatially control compositions at the microscale. Driven by entropic and enthalpic interactions, nanoparticle segregation can prevent film dewetting^{30–32}, promote defect healing^{33,34}, and fabricate a strain sensor or antenna array³⁵. Recently, structural colours have been manipulated by the interfacial segregations of melanin nanoparticles

during emulsion self-assembly^{36,37}. In bird feathers, melanosomes migrate toward the periphery of barbule cells, forming close-packed structures that reflect iridescent colours (Fig. 1a). This process is driven by depletion attraction during the late stage of keratin polymerization in feather development^{38,39}. These provide inspiration to take advantage of interfacial nanoparticle segregation to locally tune nanostructures for structural colour patterning.

In this work, we integrate photopolymerization-induced nanoparticle segregation and digital light processing (DLP) grayscale printing to achieve one-step and mask-free structural colour patterning. During photocuring, monodisperse nanoparticles in acrylic resin migrate toward the resin-substrate interface, forming a nanoparticle-segregated layer. This segregation easily occurs on oxygen-permeable substrates, and the layer thickness can be tuned from $0.37 \pm 0.02 \mu\text{m}$ to $3.21 \pm 0.09 \mu\text{m}$ by adjusting photocuring kinetics and nanoparticle

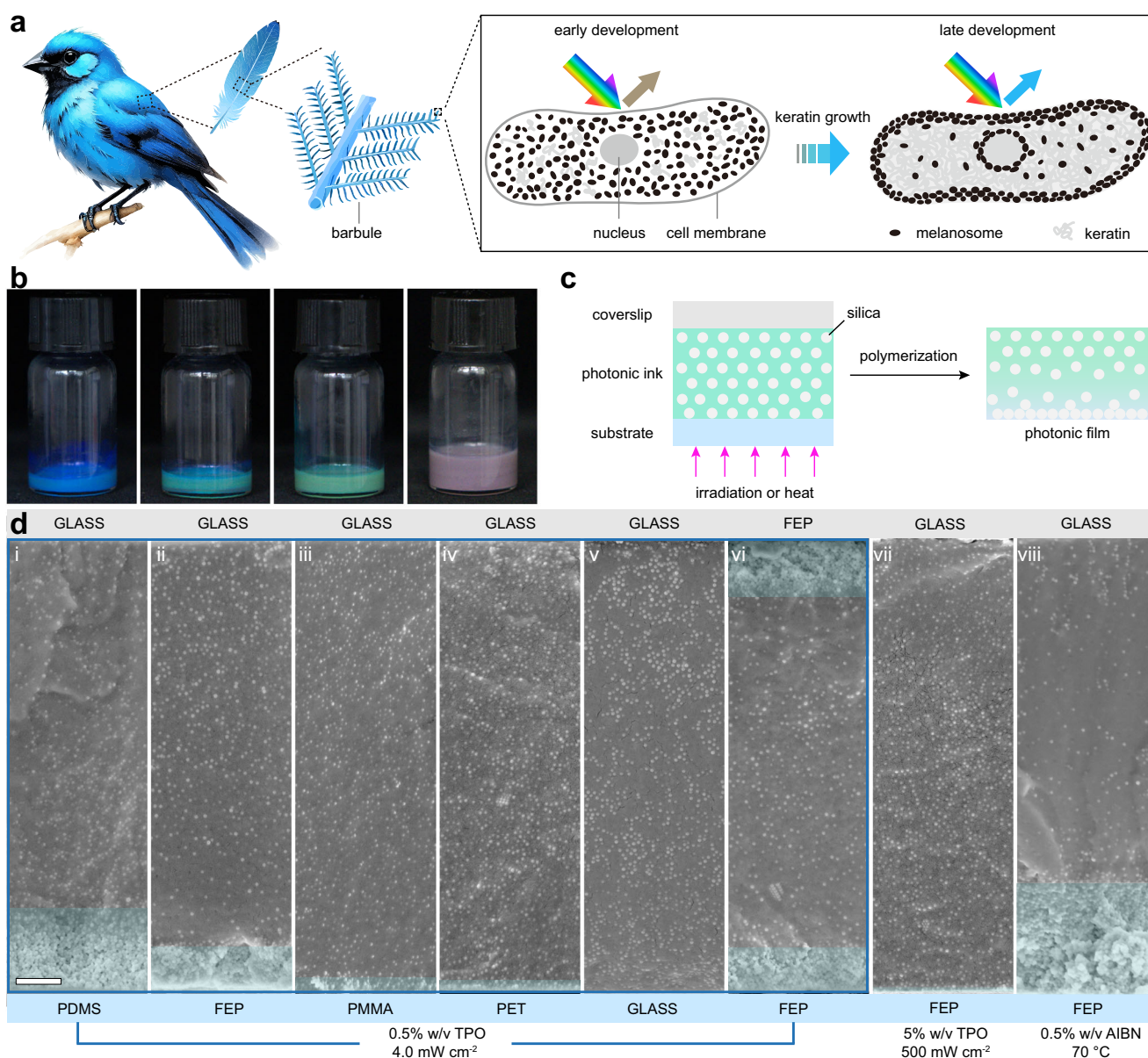


Fig. 1 | Bioinspired hierarchical structures enabled by photopolymerization-driven nanoparticle segregation. **a** Schematic of feather morphology and inner structures of barbule cells at different developmental stages in male blue-black grassquit (*Volatinia jacarina*), drawn by Li Yang inspired from the literature³⁸. **b** Photographs of photonic inks with different silica volume fractions (from left to right: 30, 25, 20, and 15%). **c** Schematic showing the preparation of the photonic film

for verifying the segregation phenomenon on different substrates. **d** Cross-sectional SEM images of polymerized films containing 15% v/v silica nanoparticles (128 nm). Films (i–vi) are cured with 0.5% w/v TPO under 4.0 mW cm^{-2} irradiance. Film (vii) is cured with 5% w/v TPO under 500 mW cm^{-2} irradiance, and film (viii) is thermally polymerized with 0.5% w/v azobisisobutyronitrile (AIBN) at $70 \text{ }^\circ\text{C}$. Scale bars, $2 \mu\text{m}$.

volume fractions. Due to the segregation layer, printed samples have Janus optical features with the segregated side exhibiting low-angle-dependent structural colours and the opposite side showing bright iridescent colours. By spatially modulating the irradiance via grayscale DLP printing, we precisely control the local segregation thickness and achieve high-resolution structural colour patterns for display or encryption. Furthermore, the microscale segregation leads to the manipulation of mid-infrared reflectivity, expanding the functionality to infrared camouflage. This work offers a versatile, scalable route to structural colour patterning for applications in anti-counterfeiting, camouflage, sensing, and display.

Results

Nanoparticle segregation driven by photopolymerization

We explore the effect of nanoparticle segregation using photocurable ink that contains monodispersed silica nanoparticles in an acrylic resin precursor. The precursor comprises ethylene glycol phenyl ether acrylate (EGPEA), 4-hydroxybutyl acrylate (HBA), poly(ethylene glycol) diacrylate (PEGDA), and diphenyl(2,4,6-trimethylbenzoyl)phosphine oxide (TPO). EGPEA is the main acrylic monomer to ensure sufficient refractive index contrast between the silica nanoparticles and the resin. HBA improves the dispersion of silica nanoparticles (Supplementary Fig. 1), PEGDA acts as a crosslinking agent, and TPO serves as a photoinitiator. To enhance colour saturation, we add a small amount of carbon black (0.015% w/w) to suppress the multiple scattering. As shown in Fig. 1b, photonic ink colour shifts from blue to pink due to increased interparticle spacing as the volume fraction decreases.

We first investigate the effect of substrate on nanoparticle segregation during photopolymerization. As shown in Fig. 1c, the photonic ink is sandwiched between a coverslip and a transparent substrate. Under UV irradiation, silica nanoparticles segregate toward the ink-substrate interface across various substrates (Fig. 1d), similarly to the segregation of melanosomes at the periphery of barbule cell membranes in bird feathers³⁸. When the substrate is polydimethylsiloxane (PDMS) and fluorinated ethylene propylene copolymer (FEP), the segregation layer thickness is $3.73 \pm 0.15 \mu\text{m}$ and $1.88 \pm 0.06 \mu\text{m}$. For poly(methyl methacrylate) (PMMA) and polyethylene terephthalate (PET), the segregation thickness decreases to $0.62 \pm 0.06 \mu\text{m}$ and $0.32 \pm 0.04 \mu\text{m}$. No segregation is observed on the glass substrate. When both the cover and substrate are FEP (Fig. 1d-vi), silica nanoparticles segregate toward both interfaces, ruling out the gravity effect and suggesting the interfacial effect caused by the substrate is the primary driver of the segregation during photopolymerization.

To explore why the degree of segregation depends on the substrate, we measure the substrate surface energy using the Owens-Wendt-Rabel-Kaelble (OWRK) method based on static contact angles of water and diiodomethane (Supplementary Table 1)⁴⁰. The measured surface energy of PDMS, FEP, PMMA, PET, and glass is 18.7 ± 0.6 , 21.4 ± 2.1 , 37.8 ± 2.3 , 39.8 ± 1.2 , and $64.2 \pm 2.7 \text{ mJ m}^{-2}$, respectively. As the substrate surface energy increases from 18.7 mJ m^{-2} to 64.2 mJ m^{-2} , the segregation layer thickness decreases from $3.73 \pm 0.15 \mu\text{m}$ to $0 \mu\text{m}$ (Supplementary Fig. 2).

We compare the enthalpy change upon segregation to examine whether the substrate surface energy is the key factor that affects the segregation. As shown in Supplementary Fig. 3, this enthalpy change is calculated by determining the interfacial energy difference between segregated and unsegregated states, $\Delta H = \gamma_{s-p} - (\gamma_{m-s} + \gamma_{m-p})$, where γ_{s-p} , γ_{m-s} , and γ_{m-p} are interfacial energies of substrate-particle, matrix-substrate, and matrix-particle. As shown in Supplementary Table 2 and Supplementary Fig. 4, ΔH is the highest for the PDMS substrate and the lowest for the glass substrate, which suggests segregation would occur onto the glass substrate instead of PDMS. This is conflicting with our experimental observations, and thus, the enthalpy effect alone does not explain the segregation phenomenon. Therefore, the segregation is not a thermodynamically controlled process.

We further conduct both fast and slow polymerization to reveal whether the nanoparticle segregation occurs before or after the polymerization. At 5% w/v photoinitiator and 500 mW cm^{-2} irradiance, rapid curing freezes the structure, resulting in a uniform distribution of silica nanoparticles in the matrix with negligible segregation even at the ink-FEP interface (Fig. 1d-vii). In contrast, thermal polymerization leads to a thicker segregation layer ($4.76 \pm 0.10 \mu\text{m}$) (Fig. 1d-viii). That is likely due to the slower curing process (~20 min), which allows sufficient time for nanoparticles to migrate toward the interface before the matrix viscosity becomes too high. These results indicate that the segregation layer forms during the polymerization, and the segregation is strongly influenced by the polymerization rate.

Inspired by previous studies that show oxygen diffusion through polymeric substrates inhibits polymerization^{41,42}, we compare the oxygen permeabilities of different substrates with the segregation thicknesses in the samples. Surprisingly, the segregation layer thickness is positively correlated with the oxygen permeability (Supplementary Fig. 5 and Table 3). To further investigate the role of oxygen, we photocure the photonic ink on an FEP film in a glovebox (oxygen concentration <1 ppm), the segregation thickness significantly decreases to $0.34 \pm 0.04 \mu\text{m}$ from $2.39 \pm 0.07 \mu\text{m}$, even under an irradiance of 0.4 mW cm^{-2} (Fig. 2a, b). When placing the substrate in a glovebox for 24 h to remove its absorbed oxygen and then starting photocuring, the segregation layer entirely disappears for both FEP and PDMS films (Fig. 2c, d).

To verify the presence of an uncured layer adjacent to the oxygen-permeable substrate due to oxygen inhibition, we irradiate the photonic ink (2 mW cm^{-2}) with varied exposure time from the FEP side in air (Fig. 2e). We observe that photopolymerization starts in the middle of the film and then gradually progress toward the coverslip first and then the FEP side. After 11 s of irradiation, the cured layer reaches and adheres to the glass coverslip, allowing us to measure the cured thickness after washing away the uncured portion adjacent to the FEP substrate. For an $86 \mu\text{m}$ -thick photonic ink, it takes 16 s to fully cure the layer. As the exposure time extends from 11 s to 16 s, the cured thickness increases from $64.2 \pm 0.7 \mu\text{m}$ to $85.7 \pm 1.0 \mu\text{m}$ (Fig. 2f). This indicates that the layer near the FEP substrate remains unpolymerized due to oxygen inhibition.

Based on the above findings, we propose that the nanoparticle segregation is caused by interfacial oxygen inhibition. As shown in Fig. 2g, oxygen diffuses through polymeric substrates into the photonic ink and its concentration decays with the distance from the substrate, as also suggested by the previous work⁴². The ink polymerizes first in regions farther away from the oxygen-permeable substrate, while the oxygen inhibits the polymerization near the substrate, generating a monomer concentration gradient between the cured and uncured regions. Such a gradient drives monomer diffusion to the cured area and nanoparticles migration towards the substrate. The degree of migration determines the segregation thickness, which depends on how rapidly the oxygen-containing region is cured.

Manipulation of segregation via 3D printing

Digital light processing (DLP) 3D printing offers customized control over photopolymerization-driven nanoparticle segregation due to its tunable light intensity, layer-by-layer resolution, and customizable printing geometries. A commercial FEP film is selected as the substrate, as it promotes nanoparticle segregation while minimizing adhesion between the printed structure and the substrate. For ease of characterization, we print a 1 mm thick slab using a layer thickness of $50 \mu\text{m}$. As shown in Fig. 3a, silica nanoparticles migrate to the ink-substrate interface during the layer-by-layer printing. The printed slab exhibits a multilayer structure, where each individual layer contains three distinct zones (Fig. 3b and Supplementary Fig. 6). In details, the nanoparticle-enriched segregation zone lies adjacent to a $\sim 10 \mu\text{m}$ nanoparticle-depleted zone, while the rest zone of the layer

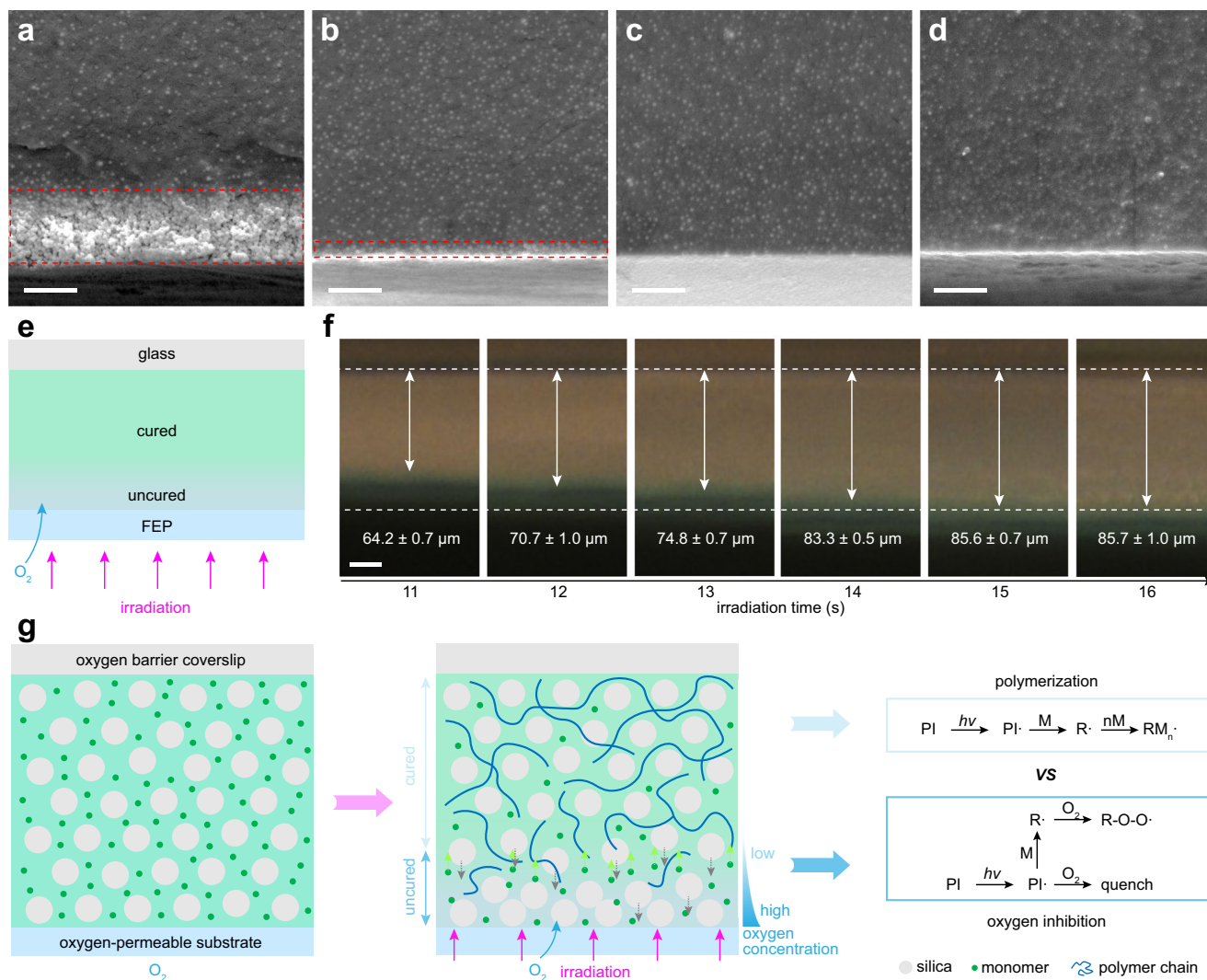


Fig. 2 | The nanoparticle segregation mechanism. a–d Influence of oxygen inhibition on the segregation thickness. Cross-sectional SEM images of samples photocured under an irradiance of 0.4 mW cm^{-2} with different conditions: **(a)** on FEP in air, **(b)** on FEP placed in a glovebox for 1 min, **(c)** on FEP placed in a glovebox for 24 h, and **(d)** on PDMS placed in a glovebox for 24 h. **e** Schematic illustration showing the cured and uncured regions during photopolymerization. The

nanoparticles are omitted in the illustration for visual clarity. **f** Optical microscopy images showing the thicknesses of the cured region under different irradiation times. **g** Schematic of the segregation mechanism resulting from oxygen inhibition. The photonic ink contains 15% v/v silica (128 nm) and 1% w/v TPO. Irradiance is 0.4 mW cm^{-2} for **(a–d)** and 2.0 mW cm^{-2} for **(f)**. Scale bar, $2 \mu\text{m}$ in **(a–d)** and $20 \mu\text{m}$ in **(f)**.

contains uniformly distributed nanoparticles (Fig. 3c and Supplementary Fig. 7).

We systematically examine how photocuring conditions affect nanoparticle segregation. As the irradiance increases from 2.0 to 28.0 mW cm^{-2} , the segregation layer thickness decreases from $2.02 \pm 0.06 \mu\text{m}$ to $0.73 \pm 0.03 \mu\text{m}$, accompanied by a gradual reduction of the adjacent nanoparticle-depleted region (Fig. 3d and Supplementary Figs. 8 and 9). A similar reduction occurs when the photoinitiator concentration increases from 0.5% to 5% w/v, leading to a decrease in segregation thickness from $2.02 \pm 0.06 \mu\text{m}$ to $0.85 \pm 0.04 \mu\text{m}$ (Supplementary Fig. 10). By regulating the irradiance and the photoinitiator concentration, we can control the photocuring rate to manipulate the segregation thickness from $0.37 \pm 0.02 \mu\text{m}$ to $2.02 \pm 0.06 \mu\text{m}$ for samples containing 15% v/v silica nanoparticles (Fig. 3e and Supplementary Fig. 11). In addition, raising the silica volume fraction from 5% to 30% produces an almost linear increase in the segregation thickness from $0.46 \pm 0.02 \mu\text{m}$ to $2.60 \pm 0.04 \mu\text{m}$ (Supplementary Figs. 12 and 13), while the particle size (128–286 nm) has little effect on segregation (Supplementary Figs. 14 and 15). Since the segregation is also observed in low volume fraction samples

without long-range order, nanoparticle segregation is largely insensitive to whether the nanoparticles form long-range ordered assemblies. Collectively, these data reveal that segregation is suppressed by faster curing kinetics but promoted by higher nanoparticle loading. A multivariable power-law fit quantitatively captures these relationships as $t_s = 11.42 c_{\text{PI}}^{-0.30} I^{-0.28} \phi^{0.96}$ ($R^2 = 0.962$), where t_s , c_{PI} , I , and ϕ represent the segregation thickness, the photoinitiator concentration, the irradiance, and the nanoparticle volume fraction (Fig. 3f). This empirical relation provides quantitative guidance for tuning segregation thickness through formulation and processing parameters.

We can further manipulate segregation using different acrylate monomers (Fig. 3g and Supplementary Fig. 16). For example, 2-hydroxyethyl methacrylate ($7.15 \pm 0.28 \mu\text{m}$) and poly(ethylene glycol) dimethacrylate ($2.09 \pm 0.04 \mu\text{m}$) lead to thicker segregation layers than 2-hydroxyethyl acrylate ($2.56 \pm 0.07 \mu\text{m}$) and poly(ethylene glycol) diacrylate ($0.50 \pm 0.02 \mu\text{m}$). This is because methacrylates have lower reactivity than acrylates and need a longer time to overcome the oxygen inhibition. As monomer functionality increases from mono- to tri-functional, the segregation thickness decreases from 2–4 μm to negligible levels. This reduction rises from faster polymerization rate

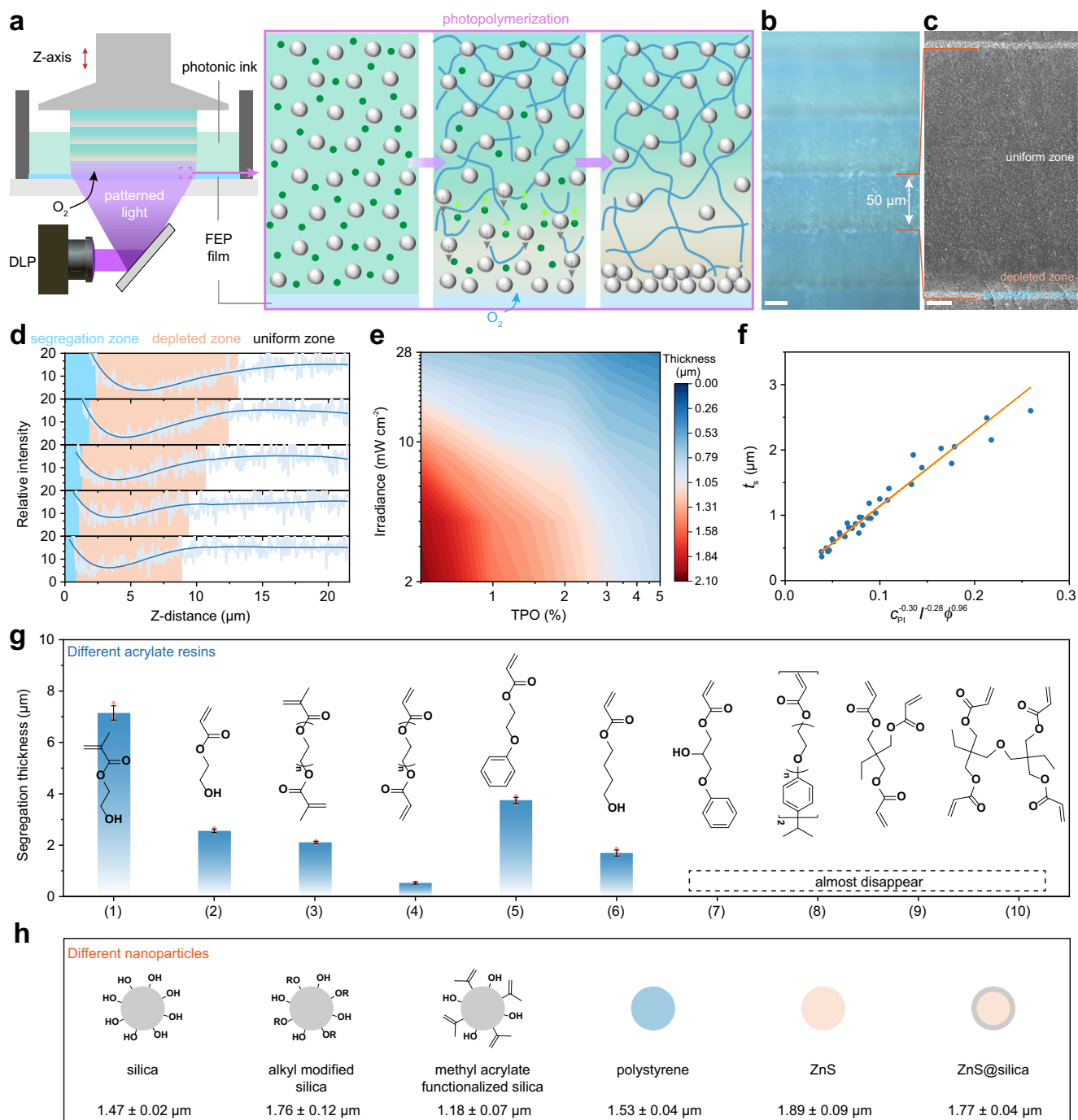


Fig. 3 | 3D printing hierarchical structures with tunable segregation.

a Schematic of the working principle of DLP printing hierarchical structures with segregation. **b** Cross-sectional optical microscopy image and **(c)** SEM image of a sample photocured with 1% w/v TPO under the irradiance of 4.0 mW cm⁻². Scale bar, 20 μm in **(b)** and 5 μm in **(c)**. **d** Vertical distribution of silica nanoparticles in a single printing layer with 0.5% w/v TPO and curing intensity ranging from 2.0, to 4.0, 11.6, 18.6, and 28.0 mW cm⁻². **e** A contour plot of segregation thickness as a function of irradiance and photoinitiator concentration. **f** A plot of segregation

thickness versus $C_{PI}^{-0.30} I^{-0.28} \phi^{0.96}$. The scattered points are experimental data and the line is based on a linear fitting with coefficient of determination of $R^2 = 0.962$. **g** Segregation thickness in different acrylic resins with 1% w/v TPO under the irradiance of 2.0 mW cm⁻². **h** Segregation thickness for samples with different nanoparticles. All the samples are made from photonic ink containing 15% v/v 128 nm silica nanoparticles. All data are presented as mean values \pm standard errors of the mean ($n = 3$).

and earlier vitrification of multifunctional acrylates that rapidly immobilize the system and suppress nanoparticle migration.

The interaction between resin and silica nanoparticles offers another route to modulate segregation. Monomers bearing hydroxyl groups, such as 2-hydroxyethyl acrylate, yield weaker segregation ($2.56 \pm 0.07 \mu\text{m}$) than non-hydroxylated monomers EGPEA ($3.75 \pm 0.12 \mu\text{m}$) (Fig. 3g). This likely rises from stronger hydrogen

bonds between monomer hydroxyl groups and surface silanols on silica compared to those formed between silanols and carbonyl or ester groups⁴³, which hinders nanoparticle mobility during photocuring. Silica nanoparticles with grafting hydrophobic alkyl chains have weaker interaction with resin and lead to slightly thicker segregation layers ($1.76 \pm 0.12 \mu\text{m}$, Fig. 3h and Supplementary Fig. 17). Conversely, silica nanoparticles grafted with methacrylate groups can chemically

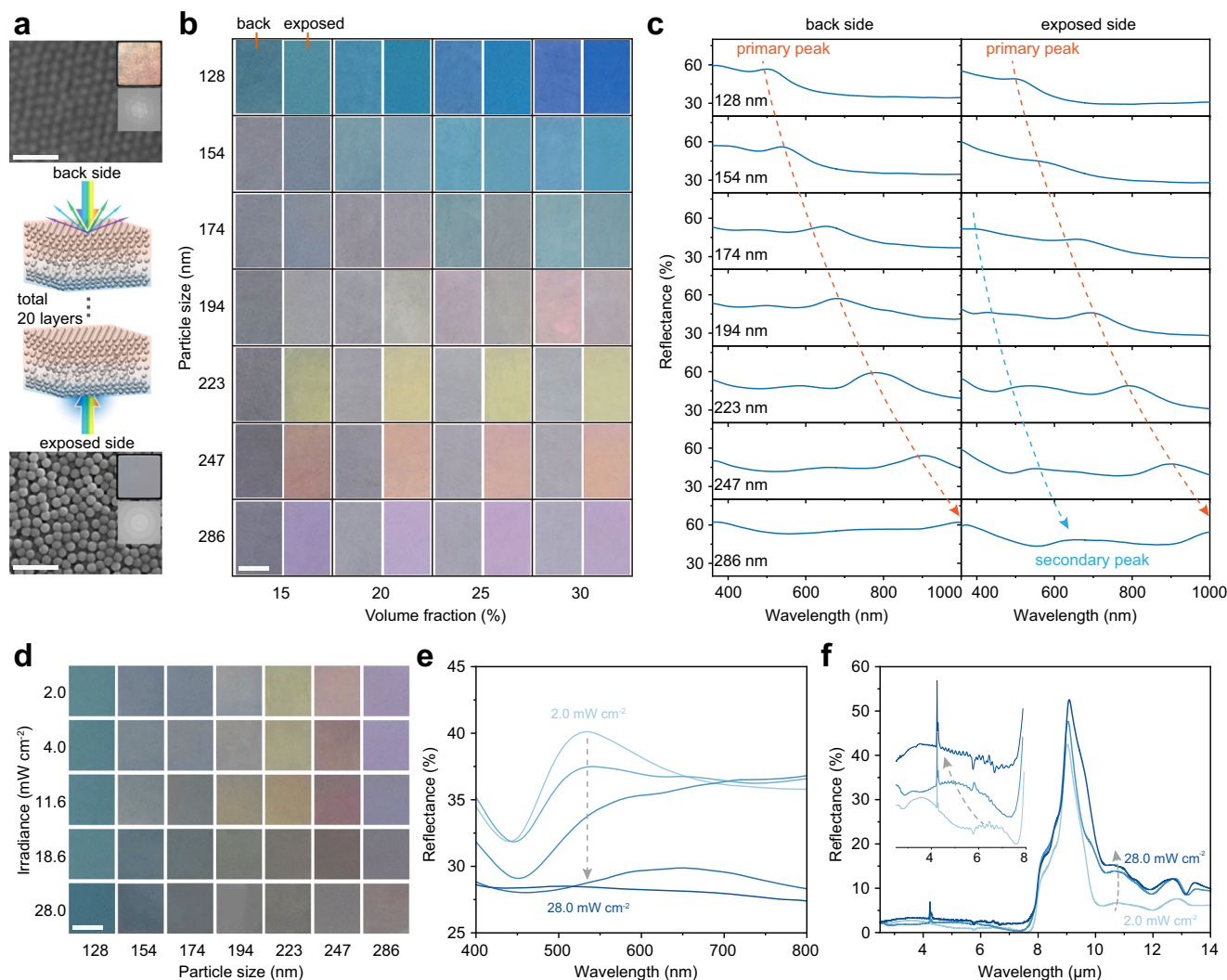


Fig. 4 | Multiple optical responses arising from nanoparticle segregation.

a Janus optical features driven by ordered structures in the back side and disordered structures in the exposed side. The photographs (0.8×0.8 cm), schematic diagram, and SEM images containing their fast Fourier transform (FFT) images are presented, respectively. **b** Optical images of both sides for samples with varying silica nanoparticle sizes and volume fractions. These samples are made from photonic ink with 1% w/v TPO and printed under the irradiance of 4.0 mW cm^{-2} . **c** Reflectance spectra of back and exposed sides for samples with different silica nanoparticle sizes at a volume fraction of 20%. **d** Optical images of the exposed side

for samples printed with varying silica nanoparticle sizes under different irradiance. These samples contain 15% v/v silica nanoparticle and 1% w/v TPO. **e** Reflectance spectra of the exposed side for the sample with 15% v/v silica nanoparticle (223 nm) and 1% w/v TPO cured under irradiance ranging from 2.0 to 4.0, 11.6, 18.6, and 28.0 mW cm^{-2} . **f** Mid-infrared reflectance spectra of samples cured under irradiance ranging from 2.0, to 11.6, and 28.0 mW cm^{-2} . Sample in **(a)** printed under the irradiance of 2.0 mW cm^{-2} . Samples in **(a)** and **(f)** are made from photonic ink containing 30% v/v silica nanoparticles (194 nm) and 1% w/v TPO. Scale bars, 1 μm in **(a)** and 3 mm in **(b, d)**.

cross-link with the matrix, which prevents nanoparticle migration and results in slightly reduced segregation ($1.18 \pm 0.07 \mu\text{m}$, Supplementary Fig. 17). When using nanoparticles such as polystyrene, zinc sulfide (ZnS), and ZnS@SiO_2 , the segregation thickness ranges from 1.53 μm to 1.89 μm (Fig. 3h and Supplementary Fig. 18). Therefore, the effect of the nanoparticle type on segregation thickness is much smaller than that of acrylate monomers and we primarily use silica to tune optical properties.

Multiple optical responses

Silica nanoparticles dispersed in acrylic resins can self-assemble into uniform long-range ordered structures once their concentration reaches a threshold, which is often regarded as being driven by the steric repulsion of solvation layers^{44,45} and electrostatic repulsion^{5,46} (Supplementary Table 4). As the silica volume increases from 5% to 30%, the arrangement of silica nanoparticles becomes more ordered as evidenced by both SEM images (Supplementary Fig. 12) and ultra-

small-angle X-ray scattering (USAXS) measurements (Supplementary Fig. 19). The disorder-order-transition occurs at approximately 15% v/v and thus we use the volume fraction above this threshold for all subsequent structurally coloured samples.

3D printed samples with nanoparticle segregation have optically distinct features on two sides. As shown in Fig. 4a, the back side, which contacts the printer platform, displays a bright metallic colour. Its reflectance spectrum shows a sharp peak, shifting from 605 nm to 536 nm as the measurement angle changes from 20° to 50° (Supplementary Fig. 20). This optical feature arises from the long-range ordered arrangement of nanoparticles, as further evidenced by the FFT image showing clear diffraction spots. In contrast, the exposed side, which faces the light source, exhibits a less saturated blue grey colour with nanoparticles packing in a disordered manner. Correspondingly, its FFT image presents concentric rings, indicating the loss of long-range order. Its reflectance spectrum contains a peak at 440 nm, remaining almost unchanged as the measurement angle

changes (Supplementary Fig. 20), consistent with the disordered arrangement.

Different levels of Janus optical features are observed across various particle sizes and volume fractions as shown in Fig. 4b. The back side shows a shift from high-wavelength (red tone) to low-wavelength (blue tone) colours with increasing volume fraction or decreasing particle size, aligning well with Bragg's law (Supplementary Fig. 21). For samples containing silica nanoparticles (128 nm) with the volume fractions increasing from 15% to 30%, the reflection peak on back side changes from 543 nm (green) to 434 nm (bluish violet) (Fig. 4b and Supplementary Fig. 22). In contrast, the colour of the exposed side is highly sensitive to the particle size but less dependent on the volume fraction. We further calculate the CIE 1976 colour difference (ΔE) between the two sides. At a volume fraction of 20%, particles between 128 nm and 174 nm yield similar colours on both sides with ΔE smaller than 5 (Supplementary Fig. 23). This is because the secondary reflectance peak of the exposed side falls in the ultraviolet range and the colour of the exposed side mainly comes from the primary reflectance peak of the ordered bulk (Fig. 4c and Supplementary Fig. 24). For larger particles (194–286 nm), the primary reflectance peak from the ordered bulk shifts toward the near infrared and it no longer contributes to the colour, while the secondary reflection from the disordered segregation layer falls within the visible spectrum. These together cause the back side to show achromatic colour (grey) while the exposed side exhibits chromatic colour, increasing ΔE up to 29.

The exposed side colour is more affected by the segregation layer compared to the back side (Supplementary Fig. 25). To tune this colour, we manipulate the segregation thickness using photonic ink containing 30% v/v silica nanoparticles (194 nm). As the irradiance increases from 2.0 mW cm⁻² to 28.0 mW cm⁻², the segregation thickness decreases from 3.21 ± 0.09 μm to 1.70 ± 0.12 μm (Supplementary Fig. 26) and the secondary reflectance peak from the disordered segregation layer weakens (Supplementary Fig. 27). The exposed side's spectrum becomes resembled that of the back side and the colour of the exposed side changes from blue to red with a colour difference of 4.8 (Supplementary Figs. 27). We may further modulate irradiance beyond the tested range to induce larger variations in segregation thickness, producing colour difference comparable to or even larger than those between the exposed and back sides in Fig. 4b.

To stand out the colour contribution of the segregation layer, we employ a low silica volume fraction of 15% while varying the particle size from 128 nm to 286 nm. This suppresses the ordered packing in the uniform zone for weak Bragg reflection while shifting the reflection peak to near infrared and making the segregation layer dominate the colour of the exposed side. Consequently, the effect of photocuring irradiance on the exposed side's colour becomes more pronounced as the particle size increases from 128 nm to 286 nm (Fig. 4d). For the samples containing 223 nm silica nanoparticles, only the secondary reflectance peak appears in the visible range. As the irradiance increases, this peak weakens and broadens, causing the colour to shift from pink to grey (Fig. 4d, e). For the grey sample, we can estimate the segregation thickness to be 0.82 μm based on the empirical relation in Fig. 3f, indicating that this thickness is too thin to produce a brilliant colour. These findings demonstrate that the colours of the exposed side can be adjusted by controlling the vertical distribution of nanoparticles through photocuring intensity.

We also examine the influence of printing thickness on the colour. As the printing thickness increases from 10 μm to 100 μm, the segregation thickness remains within the range of 2.85–3.06 μm (Supplementary Fig. 28). With a thin layer (10 μm), the exposed side's spectrum is governed by the secondary reflectance peak from the disordered segregation layer since the segregation layer dominates the structure (Supplementary Fig. 29). At 20 μm, the primary reflectance peak emerges from the ordered bulk. Beyond 50 μm, the

reflectance spectrum stabilizes, suggesting that the uppermost -50 μm determines the observed colour. Therefore, the printing thickness can be used to balance the optical contributions from the segregation layer and the underlying ordered bulk, enabling colour tuning of the exposed side.

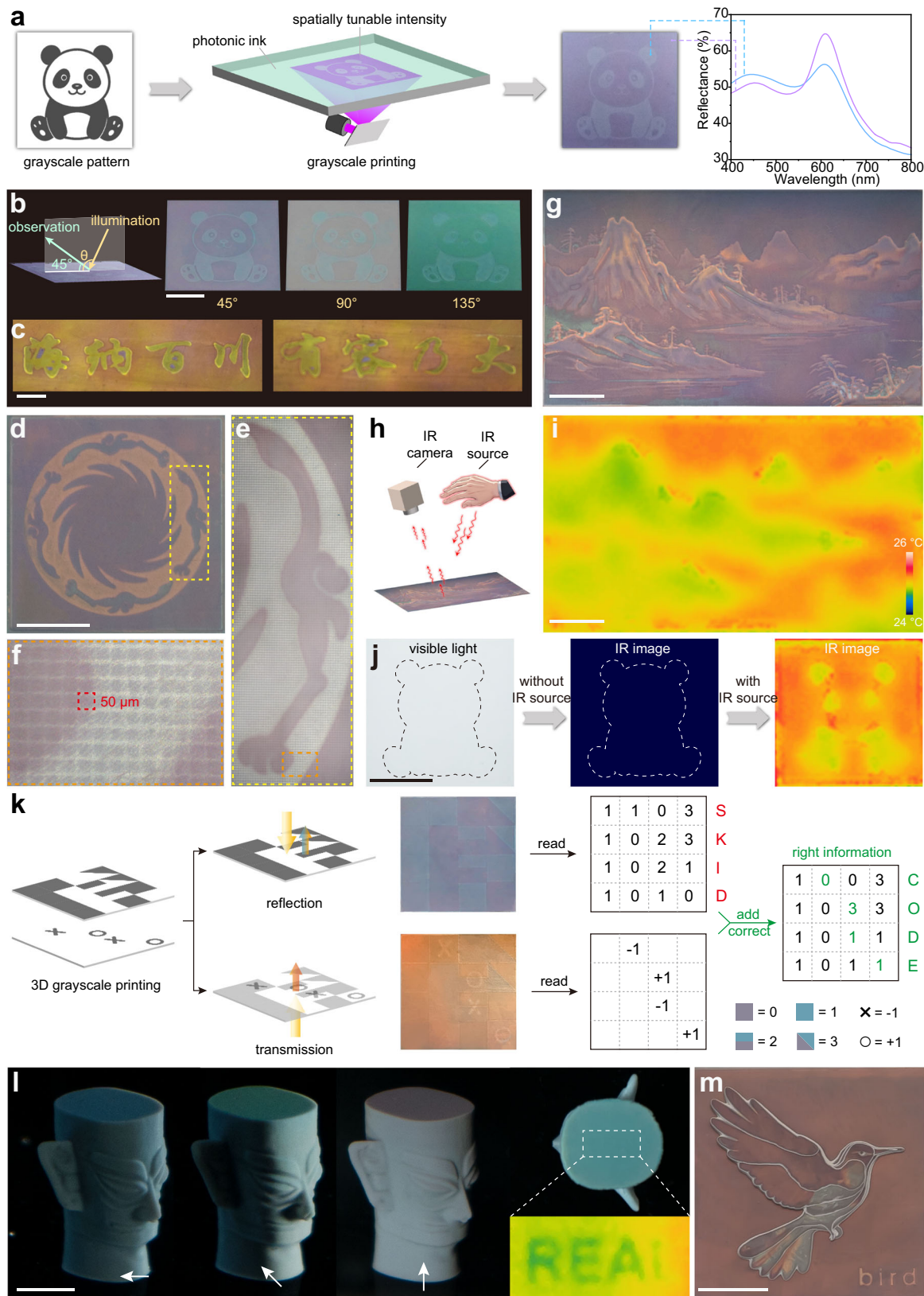
The colour quality of the printed objects is determined by both the ordered uniform and the disordered segregation zones. The packing in the segregation zone is difficult to control because of the rapid migration process during the polymerization reaction. In the uniform zone, nanoparticle arrangement remains unchanged under different photopolymerization conditions, as evidenced by the stable position of primary reflection peak across irradiance levels (Supplementary Fig. 27). This motivates us to increase the precuring time for silica nanoparticles to form a more ordered packing. Specifically, we vary the precuring time from 0 to 120 s, corresponding to the interval between lifting the printing platform and starting the photocuring of the ink. As shown in Supplementary Fig. 30, the reflectance peak becomes sharper and more intense with longer precuring time, leading to improved colour quality for both exposed and back sides. In the future work, we might try additional approaches to increase the degree of order in nanoparticle arrangements for improving colour quality, such as increasing nanoparticle surface charge⁴⁷ and decreasing the ionic strength of the medium⁴⁸. For faster processing, we still use precuring time of 0 s for the following studies.

While the structural colour originates from scattering of silica nanoparticles in visible wavelengths, the segregation layer introduces a micrometre-scale thickness comparable to mid-infrared wavelengths, prompting us to investigate its mid-infrared property. As shown in Fig. 4f, a broad, low reflectance peak shows up in the mid-wave infrared wavelengths (MWIR, 3–8 μm) while a high, sharp peak locates at 9.02 μm in the long-wave infrared wavelengths (LWIR, 8–14 μm). As the irradiance increases and the segregation layer decreases, the MWIR peak blue shifts while the intensity of the LWIR peak increases with a slight redshift.

To elucidate the underlying mechanism on the peak shift for MWIR and LWIR with segregation, we calculate the reflectance spectra of the hierarchical structures using the transfer matrix method (TMM, see Supplementary Information), which explicitly accounts for Fresnel reflections at each interface and interference within layered media⁴⁹. Each printed layer is modelled as three sublayers: a segregation zone, a nanoparticle-depleted zone, and a uniformly distributed zone (Supplementary Fig. 31). By inputting the complex refractive index for each sublayer (Supplementary Figs. 32 and 33), the calculated reflectance spectrum remains unchanged with increasing layer numbers (Supplementary Fig. 34). This suggests the reflection primarily comes from the top layer, which is consistent with the fact that the penetration depth of sample is comparable to or much less than the printing thickness (50 μm) (Supplementary Fig. 35). Using the one-layer hierarchical model, we find that the MWIR peak has a blueshift with reducing segregation thickness, while the LWIR peak slightly increases—consistent with experimental observations (Supplementary Fig. 36). These results demonstrate that controlling the segregation layer thickness provides an effective strategy to manipulate infrared reflectivity beyond visible colouration. In future work, we might optimize nanoparticle and matrix formulations for an even broader tunable range in the infrared.

Tunable structural colour patterning

Grayscale DLP printing offers pixel-level control of light intensity, providing a controllable method for spatially manipulating nanoparticle segregation to generate structural colour patterns. As displayed in Fig. 5a, a grayscale panda image is projected to locally manipulate nanoparticle segregation, resulting in a structurally coloured panda pattern. Regions exposed to higher curing intensity have weaker nanoparticle segregation and show angle-dependent



structural colour, while the low-intensity regions in the black portions of the panda pattern have strong segregation and the colours are less sensitive to viewing angles. As the illumination angle changes from 45° to 135°, the background colour turns from purple to green, whereas the colour in the black region of the panda barely changes (Fig. 5b).

This grayscale printing strategy also enables high-resolution and complex patterning. As demonstrated in Fig. 5c–g, we can print high-resolution Chinese characters (Fig. 5c), the Golden Sun Bird motif (Fig. 5d–f), and a Chinese landscape painting with colour gradients (Fig. 5g). Notably, Chinese characters on a flat film exhibit visual three-dimensionality due to optical contrast (Fig. 5c). Using the same resin

Fig. 5 | Structural colour patterning via grayscale 3D printing. **a** Schematic of grayscale printing to fabricate a panda pattern with its photograph and reflectance spectra. **b** Photographs of the printed panda pattern using photonic ink containing 30% v/v silica nanoparticles (194 nm) under different illumination angles. We fix the angle between the observation direction and the sample plane at 45° while varying the illumination angle with the sample plane (θ) from 45° to 135°. **c** Chinese characters printed using photonic ink containing 30% v/v silica nanoparticles (223 nm). **d** Photograph and **(e, f)** optical microscope image of the Golden Sun Bird motif printed using photonic ink with 30% v/v silica nanoparticles (247 nm). **g** A landscape painting printed using photonic ink with 30% v/v silica nanoparticles (247 nm). **h** Schematic showing how the infrared image is taken. **i** The infrared image of the landscape painting shown in **(g)**. **j** An anti-counterfeiting label printed

with photonic ink containing 30% v/v silica nanoparticles (194 nm). The panda pattern is invisible to both the naked eye and the IR camera under ambient conditions, but becomes detectable under IR imaging with an active IR source. **k** Schematic of information encryption based on transmitted and reflected images. The right part shows the decryption workflow for a dual-layer encoded pattern. **l** Photographs of a 3D-printed Sanxingdui bronze statue with different directions of incident light as indicated by white arrows. The right part shows the top surface has an IR anti-counterfeiting pattern. The ink contains 20% v/v silica nanoparticles (154 nm). **m** Photographs of a 3D bird-shaped label printed with 25% v/v silica nanoparticles (247 nm). All samples in **(a–j)** contain only one layer with a thickness of 150 μm . Scale bars in all photographs are 0.5 cm.

formulation and printing conditions, we can print pixels with nearly identical reflectance spectra across spatial locations and independent samples, demonstrating the reproducibility of this printing strategy (Supplementary Fig. 37). Our system can achieve a minimum structural colour pixel size of 50 μm and an image resolution of 508 ppi (Fig. 5f), which exceeds the majority of reported macroscopic structural colour patterns^{4,6,28,29}.

The resolution might be further improved higher than 508 ppi when using a DLP printer equipped with a finer DMD mirror pitch and a larger demagnification factor⁵⁰. To explore the resolution limits, we cure the ink using photomasks with pixels sizes of 12, 8, and 5 μm . Gradual changes in segregation thickness near pixel boundaries are observed, making the pixels unresolvable smaller than 8 μm (Supplementary Fig. 38). These suggest that lateral oxygen diffusion from low-irradiance to high-irradiance regions⁵¹, along with light scattering in the colloidal system⁵², can both result in slanted segregation thickness near boundaries and ultimately constrain the achievable patterning resolution.

Beyond the visible regime, nanoparticle segregation also affects infrared reflectance. With an infrared source, such as radiation from a human palm (Fig. 5h), an infrared camera can detect spatial variations in LWIR reflectivity based on local differences in segregation thickness (Fig. 5i). In the absence of active infrared illumination, the pattern becomes indistinguishable from the background (Supplementary Fig. 39). Based on this principle, we can encode information that is invisible to the naked eye but becomes detectable under infrared imaging. As shown in Fig. 5j, we use photonic ink without carbon black to print a panda pattern. This sample shows uniformly white under ambient light due to intense multiple scattering, while the pattern becomes visible under active infrared detection even in darkness.

To achieve a higher level of information encryption, we fabricate a double-layer film through layer-by-layer grayscale printing (Fig. 5k). In the reflection mode, surface features appear as visible codes, while the transmission mode reveals hidden patterns based on the transparency differences caused by nanoparticle segregation. Each pixel in the pattern is encoded as either a quaternary number or a mathematical operator. These quaternary sequences are mapped to ASCII characters. For example, (1103)₄ corresponds to “S”, (1023)₄ to “K”, (1021)₄ to “I”, (1010)₄ to “D”. Surface information alone yields an incorrect output (“SKID”), while integrating the hidden layer allows recovery of the correct message (“CODE”). This dual-layer encoding scheme demonstrates a robust strategy for secure, multi-level information storage.

We further fabricate 3D coloured objects with anti-counterfeiting patterns. As shown in Fig. 5l, we print a Sanxingdui bronze statue containing a hidden anti-counterfeiting pattern on its top surface, which is almost indistinguishable to the naked eye but clearly revealed by infrared imaging. In addition, we print a 3D bird-shaped sample where the wings and body show two different colours, brown and cyan (Fig. 5m). This strategy of combining 3D printing with 2D structural colour patterning significantly enhances the security of anti-counterfeiting labels.

Discussion

Inspired by the self-assembly of melanosomes in bird feathers, we investigate photopolymerization-induced nanoparticle segregation as a strategy for structural colour patterning. We show that nanoparticles in acrylic resin precursors undergo interfacial segregation during photopolymerization due to interfacial oxygen inhibition. By integrating DLP 3D printing, we reveal that the segregation layer thickness is governed by the photocuring rate and nanoparticle volume fraction. Thicker segregation layers can be obtained from lower light intensity, decreased photoinitiator concentration, less reactive monomers, or a higher volume fraction of nanoparticles.

Nanoparticle segregation imparts distinct Janus optical properties to the printed samples. The exposed side exhibits low angle-dependent structural colours, while the back side shows high angle-dependent colours. In addition, the colour of the exposed side highly depends on the segregation layer thickness. Through grayscale DLP printing, we can locally manipulate the segregation thickness to generate high-resolution structural colour patterns (508 ppi) from a single ink. These patterned samples demonstrate practical potential in colour display, anti-counterfeiting, and information encryption. Beyond the visible range, by tailoring the segregation thickness, we achieve tunable mid-infrared reflectivity for infrared camouflage. This one-step, mask-free, scalable approach based on nanoparticle segregation offers a versatile platform for high-resolution optical patterning across visible and infrared wavelengths. In the future, by incorporating functional nanoparticles with fluorescent, plasmonic, upconversion, IR-sensitive or thermochromic properties, we can broadly manipulate both the visible and the infrared reflectance and unlock other multifunctionalities for wide applications, including anticounterfeiting, dynamic colour modulation, camouflage, and biosensing.

Methods

Synthesis of silica nanoparticles

Silica nanoparticles were synthesized using a modified seed regrowth method⁵³. Firstly, *L*-arginine (0.1 g) was dissolved in deionized water (100 mL) in a 250 mL flask at room temperature. Tetraethyl orthosilicate (TEOS, 6.4 mL) was then added to the solution, and the mixture was heated to 70 °C with stirring for 24 h to form a silica seed dispersion. Next, ethanol (200 mL), deionized water (14 mL), ammonia solution (8 mL), and seed dispersion (1 mL) were sequentially added to a 500 mL flask under stirring at room temperature. TEOS (40 mL) was then added dropwise into the mixture under continuous stirring, and the reaction proceeded for an additional 4 h. After the reaction, we purified silica nanoparticles (128 nm) by centrifugation and ultrasonic dispersion (in ethanol) for at least four cycles. The final product was then dried at 70 °C for 24 h and redispersed in ethanol at a concentration of 10% w/v for use. By adjusting the feed ratio of the seed dispersion to TEOS, the size of silica nanoparticles was tunable from 100 to 300 nm.

Photonic ink preparation

The monomers (EGPEA and HBA), crosslinker (PEGDA), silica ethanol suspension, photoinitiator (TPO), and carbon black were thoroughly

mixed, and then placed in an oven at 70 °C for 8 h to evaporate ethanol. This yielded a structurally coloured photonic ink. Unless otherwise specified, the volume ratio of EGPEA, HBA, and PEGDA was 8:1:1, and the contents of TPO and carbon black in the acrylic resin were 1% w/v and 0.015% w/w. Following a previous report⁴⁴, the volume fraction of silica was limited to $\leq 30\%$ to prevent a liquid-to-solid transition.

Structural colour printing

Samples were printed using a commercial DLP 3D printer (M-One Pro 50, MakeX) equipped with a 405 nm light source. The exposure intensity could be adjusted from 0 to 32 mW cm⁻². The STL files were designed in AutoCAD and then converted into a series of cross-sectional images with specific slicing thicknesses (50 μm unless otherwise specified) using a slicing software (XMicro). With specific exposure intensity and layer thickness, we adjusted the curing time to achieve optimal printing accuracy. For grayscale printing, we used XMicro to convert a series of customized grayscale images into an MKP file, allowing real-time control of irradiance in each pixel. After printing, the objects were rinsed with isopropanol to remove residual ink from their surfaces. A post-curing step was performed under a 405 nm light (~50 mW cm⁻²) for 3 min.

Characterization

Scanning electron microscopy (SEM) images were taken on a Phenom Pharos G2 instrument using a secondary electron detector and an acceleration voltage of 5 kV. The samples underwent gold sputtering before observation. For each printed sample, we randomly measured the segregation thickness for at least three different layers. Static contact angle measurements were implemented on an optical contact angle measuring instrument (KRUSS DSA25) using deionized water and diiodomethane as standard probing liquids. The substrate surface energy was calculated directly by the software provided with the instrument using the OWRK method. The optical images of the samples were captured using a digital camera (Sony α7III). Optical micrographs were directly imaged using an optical microscope (Nikon LV100ND) under a dark-field mode. Reflectance spectra were recorded with an ultraviolet-visible-near-infrared microspectrophotometer (CRAIC 20/30PV Pro) with 30 W deuterium and 100 W halogen lamps for the light source. A white Teflon tape (Thorlabs, PMR10P1) was used as a white standard. We measured spectra at five different locations (82 μm × 82 μm) for each sample. Angle-resolved scattering measurements were conducted using a home-built goniometer with a deuterium-halide light source (Ideaoptics iDH2000-BSC) and an ultraviolet-visible-near-infrared spectrometer (Ideaoptics PG2000-PRO-EX). The strong peak around 655 nm in the reflectance spectra, arising from the deuterium light source, has been removed for clarity, and the original spectral data are available in the Source Data. Mid-infrared reflectance spectra were measured on an infrared microsystem (Hyperion 1000, Bruker) with a KBr beam splitter and an HgCdTe (MCT) detector. A gold mirror was used as a reflectance standard. Infrared images were taken on a FLIR T620 thermal imager with a FOL25 camera lens.

Data availability

The authors declare that the main data supporting the findings of this study are available within the article and its Supplementary Information files. Raw data have been deposited in the Zenodo database with <https://doi.org/10.5281/zenodo.18754761>. Data are available from the corresponding author upon request.

References

- Ahmed, A. et al. Bioinspired multifunctional and dynamic color-tuning photonic devices. *Chem. Rev.* **125**, 5626–5673 (2025).

- Jia, R., Xiang, S., Wang, Y., Chen, H. & Xiao, M. Electrically triggered color-changing materials: mechanisms, performances, and applications. *Adv. Opt. Mater.* **12**, 2302222 (2024).
- Zhang, Y. et al. Continuous resin refilling and hydrogen bond synergistically assisted 3D structural color printing. *Nat. Commun.* **13**, 7095 (2022).
- Xue, J. et al. Self-growing photonic composites with programmable colors and mechanical properties. *Nat. Commun.* **13**, 7823 (2022).
- Yu, S., Ma, D., Qi, C., Yang, D. & Huang, S. All-in-one photonic crystals with multi-stimuli-chromic, color-recordable, self-healable, and adhesive functions. *Adv. Funct. Mater.* **34**, 2411670 (2024).
- Miao, S., Wang, Y., Sun, L. & Zhao, Y. Freeze-derived heterogeneous structural color films. *Nat. Commun.* **13**, 4044 (2022).
- Li, L.-Y., Tan, Q.-W., Wang, X.-L., Wang, Y.-Z. & Song, F. Bioinspired hierarchical photonic structures with controllable polarization and color for optical-multiplexed information encryption. *ACS Nano* **19**, 6426–6436 (2025).
- Chen, L. et al. Peacock-inspired janus structural color materials for multi-level encryption and anti-counterfeiting. *Small* **21**, 2500024 (2025).
- Ren, J., Xie, C., Zong, H., Zhang, S. & Wu, S. Infrared stealth coating with tunable structural color based on ZnO spheres. *Small* **20**, 2403549 (2024).
- Liu, Y. et al. Cephalopod-inspired MXene-integrated mechanochromic cholesteric liquid crystal elastomers for visible-infrared-radar multispectral camouflage. *Angew. Chem. Int. Ed.* **64**, e202422636 (2025).
- Nah, S. H., Kim, J. B., Chui, H. N. T., Suh, Y. & Yang, S. Enhanced colorimetric detection of volatile organic compounds using a dye-incorporated photonic crystal-based sensor array. *Adv. Mater.* **36**, 2409297 (2024).
- Sahu, R. R. et al. Single-step fabrication of liquid gallium nanoparticles via capillary interaction for dynamic structural colours. *Nat. Nanotechnol.* **19**, 766–774 (2024).
- Xiao, M. et al. Voltage-tunable elastomer composites that use shape instabilities for rapid structural color changes. *Mater. Horiz.* **9**, 1954–1961 (2022).
- Fu, Q., Yu, W., Bao, G. & Ge, J. Electrically responsive photonic crystals with bistable states for low-power electrophoretic color displays. *Nat. Commun.* **13**, 7007 (2022).
- Xu, J. et al. Magneto-responsive cellulose nanofiber hydrogels: dynamic structuring, selective light transmission, and information encoding. *ACS Nano* **19**, 14063–14072 (2025).
- Lyu, Q., Lin, Z., Wang, P., Zhang, L. & Zhu, J. Asymmetric and ultrasensitive structural color response in nanochain-embedded photonic composites. *Adv. Opt. Mater.* **13**, 2402139 (2024).
- Chen, K., Fu, Q., Ye, S. & Ge, J. Multicolor printing using electric-field-responsive and photocurable photonic crystals. *Adv. Funct. Mater.* **27**, 1702825 (2017).
- Huang, Z., Shao, G. & Li, L. Micro/nano functional devices fabricated by additive manufacturing. *Prog. Mater. Sci.* **131**, 101020 (2023).
- Zhao, C., Wang, J., Zhang, Z. & Chi, C. Research progress on the design of structural color materials based on 3D printing. *Adv. Mater. Technol.* **8**, 2200257 (2023).
- Yang, W., Li, J., Wang, J. & Jiang, L. Bioinspired digital structural color patterning based on photonic paper/ink systems. *Adv. Funct. Mater.* <https://doi.org/10.1002/adfm.202527923> (2026).
- Llorens, J. S., Barbera, L., Demirörs, A. F. & Studart, A. R. Light-based 3D printing of complex-shaped photonic colloidal glasses. *Adv. Mater.* **35**, 2302868 (2023).
- Demirörs, A. F. et al. Three-dimensional printing of photonic colloidal glasses into objects with isotropic structural color. *Nat. Commun.* **13**, 4397 (2022).

23. Kim, J. B., Chae, C., Han, S. H., Lee, S. Y. & Kim, S.-H. Direct writing of customized structural-color graphics with colloidal photonic inks. *Sci. Adv.* **7**, eabj8780 (2021).
24. Larson, N. M. et al. Rotational multimaterial printing of filaments with subvoxel control. *Nature* **613**, 682–688 (2023).
25. Liu, K. et al. 3D printing colloidal crystal microstructures via sacrificial-scaffold-mediated two-photon lithography. *Nat. Commun.* **13**, 4563 (2022).
26. Wang, J. et al. Nanograting-based dynamic structural colors using heterogeneous materials. *Nano Micro Lett.* **17**, 59 (2025).
27. Li, K. et al. Facile full-color printing with a single transparent ink. *Sci. Adv.* **7**, eabh1992 (2021).
28. Liao, J. et al. 3D-printable colloidal photonic crystals. *Mater. Today* **56**, 29–41 (2022).
29. Jeon, S. et al. Direct-ink-write cross-linkable bottlebrush block copolymers for on-the-fly control of structural color. *Proc. Natl. Acad. Sci. USA* **121**, e2313617121 (2024).
30. Luo, H. & Gersappe, D. Dewetting dynamics of nanofilled polymer thin films. *Macromolecules* **37**, 5792–5799 (2004).
31. Xue, L. & Han, Y. Inhibition of dewetting of thin polymer films. *Prog. Mater. Sci.* **57**, 947–979 (2012).
32. Roy, S., Bandyopadhyay, D., Karim, A. & Mukherjee, R. Interplay of substrate surface energy and nanoparticle concentration in suppressing polymer thin film dewetting. *Macromolecules* **48**, 373–382 (2015).
33. Tyagi, S., Lee, J. Y., Buxton, G. A. & Balazs, A. C. Using nano-composite coatings to heal surface defects. *Macromolecules* **37**, 9160–9168 (2004).
34. Gupta, S., Zhang, Q., Emrick, T., Balazs, A. C. & Russell, T. P. Entropy-driven segregation of nanoparticles to cracks in multilayered composite polymer structures. *Nat. Mater.* **5**, 229–233 (2006).
35. Deore, B. et al. Direct printing of functional 3D objects using polymerization-induced phase separation. *Nat. Commun.* **12**, 55 (2021).
36. Heil, C. M. et al. Mechanism of structural colors in binary mixtures of nanoparticle-based supraballs. *Sci. Adv.* **9**, eadf2859 (2023).
37. Xiao, M. et al. Experimental and theoretical evidence for molecular forces driving surface segregation in photonic colloidal assemblies. *Sci. Adv.* **5**, eaax1254 (2019).
38. Maia, R., Macedo, R. H. F. & Shawkey, M. D. Nanostructural self-assembly of iridescent feather barbules through depletion attraction of melanosomes during keratinization. *J. R. Soc. Interface.* **9**, 734–743 (2012).
39. Nordén, K. K., Eliason, C. M. & Stoddard, M. C. Evolution of brilliant iridescent feather nanostructures. *ELife* **10**, e71179 (2021).
40. Owens, D. K. & Wendt, R. C. Estimation of the surface free energy of polymers. *J. Appl. Polym. Sci.* **13**, 1741–1747 (1969).
41. Dendukuri, D. et al. Modeling of oxygen-inhibited free radical photopolymerization in a PDMS microfluidic device. *Macromolecules* **41**, 8547–8556 (2008).
42. Tumbleston, J. R. et al. Continuous liquid interface production of 3D objects. *Science* **347**, 1349–1352 (2015).
43. Raghavan, S. R., Walls, H. J. & Khan, S. A. Rheology of silica dispersions in organic liquids: new evidence for solvation forces dictated by hydrogen bonding. *Langmuir* **16**, 7920–7930 (2000).
44. Kim, J. B., Lee, H., Chae, C., Lee, S. Y. & Kim, S. Advanced additive manufacturing of structurally-colored architectures. *Adv. Mater.* **36**, 2307917 (2023).
45. Lee, G. H. et al. Chameleon-inspired mechanochromic photonic films composed of non-close-packed colloidal arrays. *ACS Nano* **11**, 11350–11357 (2017).
46. Hu, Y., Qi, C., Ma, D., Yang, D. & Huang, S. Multicolor recordable and erasable photonic crystals based on on-off thermoswitchable mechanochromism toward inkless rewritable paper. *Nat. Commun.* **15**, 5643 (2024).
47. Xing, Y., Fei, X. & Ma, J. Ultra-fast fabrication of mechanical-water-responsive color-changing photonic crystals elastomers and 3D complex devices. *Small* **20**, 2405426 (2024).
48. Fan, Q. et al. Unveiling enhanced electrostatic repulsion in silica nanosphere assembly: formation dynamics of body-centered-cubic colloidal crystals. *J. Am. Chem. Soc.* **145**, 28191–28203 (2023).
49. Byrnes, S. J. Multilayer optical calculations. Preprint at <https://doi.org/10.48550/arXiv.1603.02720> (2020).
50. Chekkaramkodi, D., Jacob, L., Muhammed Shebeeb, C., Umer, R. & Butt, H. Review of vat photopolymerization 3D printing of photonic devices. *Addit. Manuf.* **86**, 104189 (2024).
51. Kim, S., Lee, H., Choi, H., Yoo, K.-Y. & Yoon, H. Investigation on photopolymerization of PEGDA to fabricate high-aspect-ratio microneedles. *RSC Adv* **12**, 9550–9555 (2022).
52. Korčušková, M., Lepcio, P. & Jančář, J. Metal oxide-functionalized photopolymers: a perspective in 3D printing. *ACS Polym. Au* **5**, 458–480 (2025).
53. Watanabe, R. et al. Extension of size of monodisperse silica nanospheres and their well-ordered assembly. *J. Colloid Interface Sci.* **360**, 1–7 (2011).

Acknowledgements

M.X. acknowledges financial support from the National Natural Science Foundation of China (52203273), the State Key Laboratory of Polymer Materials Engineering (sklpme2023-2-14), the Fundamental Research Funds for the Central Universities, and the Beamtime Key Project at the Shanghai Synchrotron Radiation Facility (2024 SSRF ZD 508355). We thank Dong Yang, Shuhong Xiang, Xiuhua Yang, Fanglin Guo, Zhengyu Li, Chengjie Zhang, Qin Li, Yanxuan Fu, and Ye Yuan for their comments on the manuscript. We thank Kai Wu for using the thermal imager in his lab and Cong Guo for his assistance. We thank Hao Zhang (Shanghai Advanced Research Institute, Chinese Academy of Sciences) for his technical assistance with USAXS measurements.

Author contributions

L.Y. and M.X. conceived the idea and designed the experiments. L.Y., Y.P., and Z.W. performed experiments. L.Y. and M.X. wrote the original manuscript. L.Y., Y.P., Z.W., W.W., Y.W., and M.X. revised the manuscript. M.X. supervised the project and acquired the funding.

Competing interests

M.X. and L.Y. are inventors on a Chinese patent application (application number 202510664587.4, filed on May 22, 2025) related to the fabrication of hierarchical photonic structures based on nanoparticle segregation, and they declare no other competing interests. The remaining authors declare no competing interests.

Additional information

Supplementary information The online version contains supplementary material available at <https://doi.org/10.1038/s41467-026-70490-4>.

Correspondence and requests for materials should be addressed to Ming Xiao.

Peer review information *Nature Communications* thanks Yanlin Song and the other anonymous reviewers for their contribution to the peer review of this work. A peer review file is available.

Reprints and permissions information is available at <http://www.nature.com/reprints>

Publisher's note Springer Nature remains neutral with regard to jurisdictional claims in published maps and institutional affiliations.

Open Access This article is licensed under a Creative Commons Attribution 4.0 International License, which permits use, sharing, adaptation, distribution and reproduction in any medium or format, as long as you give appropriate credit to the original author(s) and the source, provide a link to the Creative Commons licence, and indicate if changes were made. The images or other third party material in this article are included in the article's Creative Commons licence, unless indicated otherwise in a credit line to the material. If material is not included in the article's Creative Commons licence and your intended use is not permitted by statutory regulation or exceeds the permitted use, you will need to obtain permission directly from the copyright holder. To view a copy of this licence, visit <http://creativecommons.org/licenses/by/4.0/>.

© The Author(s) 2026